10.1021/jp004586n

A Study of the Formation of Single- and Double-Walled Carbon Nanotubes by a CVD Method

Alain Peigney,[†] Pierre Coquay,[‡] Emmanuel Flahaut,[†] Robert E. Vandenberghe,[‡] Eddy De Grave,[‡] and Christophe Laurent*,[†]

CIRIMAT UMR CNRS 5085 / LCMIE, Centre Interuniversitaire de Recherche et d'Ingénierie des Matériaux, Université Paul-Sabatier, 31062 Toulouse Cedex 4, France and NUMAT, Department of Subatomic and Radiation Physics, Ghent University, Proeftuinstraat 86, B-9000 Gent, Belgium

The reduction in H_2/CH_4 atmosphere of aluminum−iron oxides produces metal particles small enough to catalyze the formation of single-walled carbon nanotubes. Several experiments have been made using the same temperature profile and changing only the maximum temperature (800−1070 °C). Characterizations of the catalyst materials are performed using notably ^{57}Fe Mössbauer spectroscopy. Electron microscopy and a macroscopical method are used to characterize the nanotubes. The nature of the iron species (Fe^{3+}, α-Fe, γ-Fe−C, Fe_3C) is correlated to their location in the material. The nature of the particles responsible for the high-temperature formation of the nanotubes is probably an Fe−C alloy which is, however, found as Fe_3C by postreaction analysis. Increasing the reduction temperature increases the reduction yield and thus favors the formation of surface-metal particles, thus producing more nanotubes. The obtained carbon nanotubes are mostly single-walled and double-walled with an average diameter close to 2.5 nm. Several formation mechanisms are thought to be active. In particular, it is shown that the second wall can grow inside the first one but that subsequent ones are formed outside. It is also possible that under given experimental conditions, the smallest (<2 nm) catalyst particles preferentially produce double-walled rather than single-walled carbon nanotubes.

Introduction

The report by Iijima[1] on carbon nanotubes (CNTs) prompted a significant research effort on their synthesis, their structure, and the study and measurement of their properties. An increasing fraction of the research work is now driven by the very high potential of CNTs, notably single-walled carbon nanotubes (SWNTs), for technological applications. This requires the availability of large quantities of CNTs of well-determined and reproducible characteristics. Understanding the formation mechanisms of the CNTs is therefore a key issue for the development of further research in this topic.

Several mechanisms have been proposed (see Laurent et al.[2] for a review), involving the interaction of carbon species with a metal in a different form (atom, cluster, nanoparticle, etc.) depending on the synthesis method. Chemical methods known as catalytic chemical vapor deposition (CCVD) are becoming increasingly attractive because of their great potential for the production of large quantities at a low cost. These methods are basically similar to those used for several decades for the synthesis of various filamentous forms of carbon, including hollow fibers (see Rodriguez[3] for a review). They involve the catalytic decomposition of hydrocarbons or carbon monoxide on transition-metal particles, the major difference lying in the catalyst material itself. As opposed to the production of hollow carbon fibers, to obtain SWNTs, the size of the metal particles has to be very small (a few nanometers in diameter). The formation mechanisms are also different. A crucial difficulty thus is to design a way to obtain nanometric metal particles at the temperature (usually higher than 700 °C) required for the formation of CNTs by CCVD methods.

The present authors have proposed an original CCVD method based on the selective reduction of oxide solid solutions in a H_2/CH_4 gas mixture.[4] The reduction of α-$Al_{1.9}Fe_{0.1}O_3$ produces pristine Fe nanoparticles at a temperature high enough for them to catalyze the decomposition of CH_4 and the in-situ formation of CNTs. The so-obtained powders contain an enormous amount of SWNTs and MWNTs (multiwalled carbon nanotubes). Several parameters related to the catalyst material have been investigated to increase the proportion of SWNTs. They include the iron content,[5] the crystallographic form,[6] and the specific surface area[7] of alumina-based solid solutions. The nature of the metallic phase (Fe, Co, Ni, and their binary alloys) was also investigated[8,9] using $MgAl_2O_4$-based solid solutions. The so-obtained products are CNTs-metal-oxide composite powders with a very homogeneous dispersion of the CNTs that cannot be matched by methods involving a mechanical mixing. Dense ceramic-matrix composites have been prepared from such powders, showing acceptable mechanical properties in addition to an electrical conductivity of the order of 1 S/cm because of the percolation of the CNTs network.[10,11] Furthermore, it was also shown that when using Co−MgO catalysts, a simple soaking in HCl allows to separate the CNTs from the catalyst materials without damaging them.[12] The so-obtained CNTs, 90% of which are SWNTs and DWNTs (double-walled carbon nanotubes), are individually dispersed in the matrix rather than in bundles and have a very high specific surface area (ca. 950 m^2/g for carbon).[13] The diameter distribution spreads in the range

* To whom correspondence should be addressed. Tel.: 33 (0)5 61 55 61 22. Fax: 33 (0)5 61 55 61 63. E-mail: laurent@chimie.ups-tlse.fr.
† Université Paul-Sabatier.
‡ Ghent University.

0.5−5 nm, and more than 90% have a diameter lower than 3 nm, which is in excellent agreement with the theoretical and experimental results reported by Hafner et al.[14]

The effects upon the CNT formation of some parameters related to the experimental conditions of the reduction, such as the composition of the H_2/CH_4 atmosphere,[15] the reduction temperature (T_r), and the time spent at that temperature[16] have also been examined. In particular, the increase of T_r from 900 to 1000 °C, using the same composition of the reducing atmosphere, was found[5,6] to produce an increase in the amount of CNTs but was also found to favor tube thickening and the deposition of nontubular carbon species.

Obviously, the influence of the temperature depends on the nature of the carbonaceous gas. Dai et al.[17] reported the formation of SWNTs together with a small amount of DWNTs by disproportionation of CO at 1200 °C on Al_2O_3-supported Mo particles. The SWNTs, 1−5 nm in diameter, are found with a single catalytic particle of commensurate diameter located at the tip. Larger particles are covered by a few graphene layers and are inactive for the CNT formation. Hafner et al.[14] synthesized a mixture of SWNTs and DWNTs by catalytic decomposition of C_2H_4 at 700−850 °C over Mo− and Fe/Mo−Al_2O_3 catalysts. They report that the DWNT proportion increases from 30% at 700 °C to 70% at 850 °C. Ivanov et al.[18] reduced a zeolite-supported Co catalyst in N_2–C_2H_2 and obtained a small amount of MWNTs (2−3 walls) 4 nm in diameter together with much thicker tubes. Increasing the T_r from 500 to 800 °C results in the deposition of more amorphous carbon and in a better crystallinity of the concentric graphite layers. Hernadi et al.[19] passed N_2/hydrocarbon (acetylene, ethylene, propylene, and methane) gas mixtures over Fe−SiO_2 catalyst at 700, 750, and 800 °C, and they notably report that, at 700 °C, the MWNT quality is higher when using acetylene and that no carbon at all is deposited when using methane. Colomer et al.[20] reported the synthesis of individual CNTs and bundles of SWNTs at 1080 °C in N_2/C_2H_4 over (Fe, Co, Ni) particles dispersed on Al_2O_3/SiO_2 substrate. Similar results were achieved[21] at 1000 °C in H_2/CH_4 over a Co−MgO catalyst. Cassell et al.[22] claimed to have prepared gram quantities of SWNTs free of defects and of amorphous-carbon coating by CCVD of CH_4 at 900 °C on an Fe/Mo catalyst supported on a new Al_2O_3/SiO_2 hybrid material. DWNTs are also present but their proportion is considered negligible. Other researchers[23,24] have also reported the synthesis of SWNTs by decomposition of CH_4 at 800−1000 °C over various catalysts. Cheng et al.[25] prepared ropes of SWNT bundles by decomposition of ferrocene−thiophene−benzene−hydrogen mixtures at 1100−1200 °C and reported the presence of impurities such as carbon nanoparticles and catalyst particles.

The aim of the present paper is to study the influence of the temperature on the CNT formation by reduction of an α-$Al_{1.8}Fe_{0.2}O_3$ solid solution in H_2/CH_4. One of the notable effects of increasing the temperature while maintaining constant the composition of the reducing atmosphere is that the CH_4 supersaturation level increases[26] until the maximum temperature is reached.

The obtained materials have a fairly complex microstructure with several iron species of various sizes dispersed inside and at the surface of the alumina matrix and with several carbon species including SWNTs. Characterizations are performed on one hand for the catalyst material before and after reduction using mainly ^{57}Fe Mössbauer spectroscopy, and on the other hand for the CNTs using electron microscopy as well as a macroscopical method based on specific-surface-area measurements. It is attempted first to correlate the nature of the iron species to their location in the material and to determine which are active for the CNT formation and second to investigate the formation mechanisms.

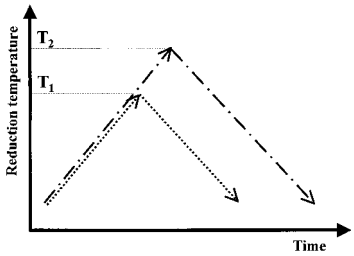

Figure 1. Sketch showing the temperature profile of two runs (at T_1 and at T_2) in H_2/CH_4 atmosphere.

Experimental Section

Synthesis of Carbon Nanotubes. An α-$Al_{1.8}Fe_{0.2}O_3$ powder was prepared by decomposition in air at 400 °C and further calcination at 1000 °C of the corresponding mixed-oxalate as described elsewhere.[27] The powder is made up of 10−20 μm agglomerates of submicronic or nanometric primary grains. Its specific surface area S_{ss} is equal to 9.0 ± 0.3 m^2/g. Several batches of the solid-solution powder were reduced in a H_2/CH_4 gas mixture. The heating/cooling rate to the desired temperature (T_r = 800, 850, 910, 990, 1050, and 1070 °C) and back to room temperature was 5 °C/min. No dwell was applied at T_r. Note that because the heating/cooling rate is small, one cannot consider that all runs are dependent upon T_r only. On the contrary, a run at a given T_r is an extension of an experiment performed at a lower T_r, as illustrated in Figure 1. The composition of the gas mixture (18 mol % CH_4) was chosen from the results of a previous study.[15] The flowing gas was dried on P_2O_5, and its composition was regulated by massflow controllers. The flow rate was fixed at 250 sccm. For the sake of brevity, the so-obtained CNTs-Fe/Fe_3C−Al_2O_3 powders will hereafter be denoted as R800, R850, R910, R990, R1050, and R1070, according to the corresponding T_r.

Characterization. The powders were studied using conventional scanning and transmission electron microscopy and high-resolution transmission electron microscopy (SEM, TEM, and HREM, respectively), X-ray diffraction (XRD) using Co−K_α radiation (λ = 0.17902 nm), and ^{57}Fe Mössbauer spectroscopy. The Mössbauer spectra (MS) were recorded with a ^{57}Co (Rh) source with a conventional time-mode spectrometer with a constant-acceleration drive and a triangular reference signal. Accumulation of the data was performed in 1024 channels until a background of at least 10^6 counts per channel was reached. The spectrometer was calibrated by collecting at room temperature the spectrum of a standard α-Fe foil, and the isomer-shift values quoted hereafter are with reference to this standard. The measured absorbers were prepared with the amount of powder corresponding to 10 mg of iron atoms per square centimeter. The spectra were generally analyzed assuming symmetrical components with Lorentzian line shapes. However, asymmetrical Mössbauer patterns were fitted with a model-independent hyperfine-field or a quadrupole-splitting distribution with Lorentzian shaped elemental subspectra. The quoted isomer-shift and quadrupole-shift values are in that case average values for the distributed parameters. Measurements between 14 K and RT were performed using a closed-cycle refrigerator.

Macroscopical Evaluation of the CNT Quantity and of the Carbon-Species Characteristics. In addition to the electron-microscopy characterizations, a method based on chemical

analysis and specific-surface-area measurements[4,6,28] was used to characterize the composites at a macroscopical scale and thus produce data which are more representative of the material than those derived from local techniques. Two parameters representing the quantity of CNTs and what is called the quality of the deposited carbon are calculated, a higher quality parameter principally corresponding to more carbon in tubular form or CNTs with fewer walls or less bundled CNTs. Parts of the CNTs-Fe/$Fe_3C-Al_2O_3$ powders were oxidized in air at 900 °C to eliminate all the carbon, as required for the specific-surface-area study. The specific surface areas of the powders obtained after reduction (S_n) and of the specimens oxidized at 900 °C (S_o) were measured by the BET method using N_2 adsorption at liquid N_2 temperature in a Micromeritics FlowSorb II 2300 apparatus. This instrument gives a specific-surface-area value from one point (i.e., one adsorbate pressure) and requires calibration. The reproducibility of the results was determined to be in the ±3% range. The carbon content was determined by flash combustion with an accuracy of ±2%.

Results and Discussion

X-ray Diffraction. The XRD pattern of the oxide shows the presence of a small proportion of α-Fe_2O_3 besides the peaks of the alumina-hematite solid solution in the corundum (α) form. This reveals that the crystallization from the metastable oxide solid solution takes place with some degree of phase partitioning, producing a mixture of alumina-rich (α_1, major phase) and hematite-rich (α_2, minor phase) corundum forms. The solubility limit of α-Fe_2O_3 in α-Al_2O_3 in the present experimental conditions is thus below 10 cat. % Fe^{3+} (i.e., $x < 0.1$ in α-$Al_{2-2x}Fe_{2x}O_3$). Other workers have reported various solubility limits when using other synthesis routes.[29−31] The reduction in pure H_2 of the α_2 phase is known[27,32] to be relatively easy and to produce fairly large Fe particles (10−30 nm) located at the surface of the Al_2O_3 (or partially reduced α_1) grains, whereas the H_2 reduction of the α_1 phase produces nanometric Fe particles (<10 nm) located both inside and at the surface of the matrix grains. The size distribution of the Fe particles is thus bimodal.

Analysis of the XRD patterns of the present reduced powders reveals the increasing presence of α-Fe and Fe_3C upon the increase in T_r besides a corundum phase accounting for α-Al_2O_3 or a partially reduced α-$Al_{2-2y}Fe_{2y}O_3$ ($y < 0.1$) solid solution (corresponding to the above-mentioned α_1 phase in the unreduced material). It is difficult to clearly separate the patterns of α-Fe and Fe_3C because the peaks are rather wide and overlap. The absence of the α-Fe_2O_3 peaks even for a low T_r indicates the complete reduction of the α_2 phase in agreement with earlier studies.[27,32] γ-Fe or a γ-Fe−C alloy may also be present, but cannot be resolved on the XRD patterns because the γ-Fe (111) diffraction peak ($d_{111} = 0.208$ nm) is masked by the corundum (113) ($d_{113} = 0.209$ nm) and the Fe_3C (121) ($d_{121} = 0.210$ nm) peaks.

^{57}Fe Mössbauer Spectroscopy. The oxide powder was measured at 80 K and at RT (Table 1 and Figure 2). The MS were fitted with a doublet accounting for Fe^{3+} and a sextet, which can be attributed to a magnetic phase of α-Fe_2O_3. The sextet clearly shows a hyperfine-field distribution, and ranges 500−550 kOe and 480−530 kOe were used in the fits of the MS at 80 K and RT, respectively. The evaluated distribution profiles clearly show a tail toward low-field values. The proportion of the sextet is higher at 80 K than at RT, and this feature suggests a size distribution of the particles, the smallest ones exhibiting superparamagnetic relaxation down to at least 80 K. Superparamagnetic α-Fe_2O_3 particles at RT are typically smaller than 10 nm.[33] Such small sizes also explain why most of them do not show the Morin transition (and hence remain weakly ferromagnetic) even at 80 K, as proved by the negative value of the average quadrupole shift ($\overline{\epsilon_Q} = -0.15$ mm/s) at that temperature. The sextet thus mostly represents hematite particles (α_2 phase) formed by phase partitioning during the crystallization as mentioned in the above XRD section. The doublet represents Fe^{3+} ions substituting for Al^{3+} ions in the alumina-rich corundum (α_1) lattice and also the α-Fe_2O_3 particles (α_2) that are superparamagnetic at the measurement temperature. However, the Fe^{3+} ions in the α_1 lattice may also give rise to a hematite sextet, depending on the measurement temperature and the degree of their agglomeration.

The MS of R800 (a), R850 (b), R910 (c), R990 (d), and R1070 (e) measured at 80 K are shown in Figure 3 and the adjusted parameters at 80 K and at RT are given in Tables 2 and 3, respectively. The α-Fe_2O_3 phase is not detected in these spectra, even not for R800, in agreement with the XRD results. Besides the Fe^{3+} doublet, two sextets and a singlet were used to fit the spectra. The more intense sextet accounts for ferromagnetic α-Fe and the weaker one for ferromagnetic Fe_3C (cementite).[34] The singlet corresponds to a nonferromagnetic iron phase. Considering the MS proportions at 80 K with increasing T_r (Figure 4a and Table 2), it appears that the proportions of Fe^{3+} gradually decrease, that the proportions of Fe_3C and of the singlet phase increase, and that the proportions of α-Fe at first decrease and subsequently increase. The RT MS (Figure 4b and Table 3) reflects the same trends but with a shift of the α-Fe proportions toward lower values in favor of the Fe^{3+} proportions.

TABLE 1: MS Parameters of the $Al_{1.8}Fe_{0.2}O_3$ Oxide Powder Measured at 80 K and at RT[a]

	weakly ferro α-Fe_2O_3					superpara Fe^{3+}			
T (K)	$\overline{\delta}$	H_{hf}	$\overline{2\epsilon_Q}$	Γ	P	δ	ΔE_Q	Γ	P
80[b]	0.47	530	−0.15	0.31	12	0.40	0.55	0.40	88
RT[c]	0.35	510	−0.22	0.21	6	0.29	0.55	0.37	94

[a] Weakly ferro: weakly ferromagnetic; superpara: superparamagnetic; H_{hf}: hyperfine field at the maximum of the distribution (kOe); $\overline{\delta}$: (average) isomer shift (mm/s); ΔE_Q: quadrupole splitting (mm/s); $\overline{2\epsilon_Q}$: average quadrupole shift (mm/s); Γ: Lorentzian line width (mm/s); P: proportion (%). [b] Hyperfine-field distribution from 500 to 550 kOe. [c] Hyperfine-field distribution from 480 to 530 kOe.

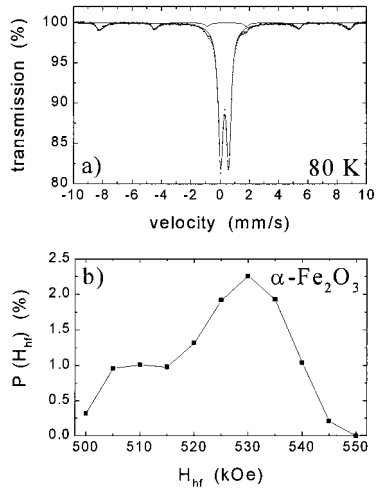

Figure 2. MS (a) and α-Fe_2O_3 hyperfine-field distribution (b) of the $Al_{1.8}Fe_{0.2}O_3$ oxide powder measured at 80 K.

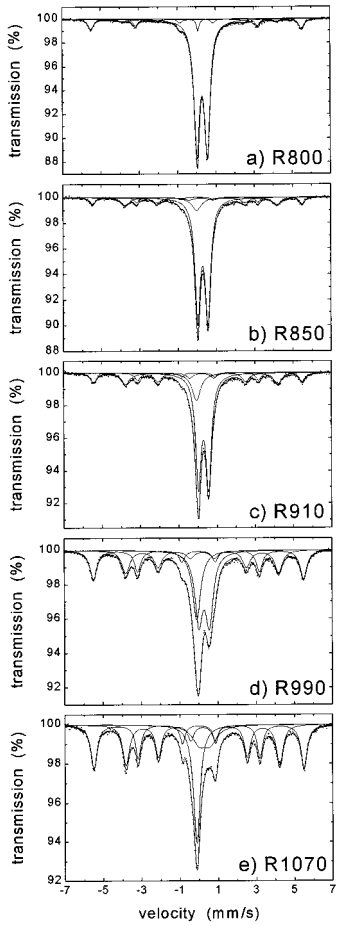

Figure 3. MS of R800 (a), R850 (b), R910 (c), R990 (d), and R1070 (e) measured at 80 K.

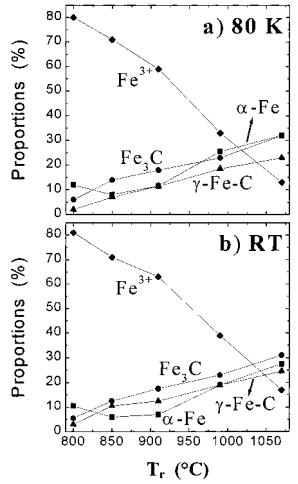

Figure 4. Proportions of the iron phases in the reduced powders as calculated from the MS measured at 80 K (a) and at RT (b) vs the reduction temperature (T_r) of the specimen.

To obtain more information about the iron phases and the variation of their proportions, R990 was studied at different temperatures between 14 K and RT (Figure 5 and Table 4). Up to 75 K, a distributed sextet was included in the fit in addition to the four patterns detected at RT and at 80 K. Its hyperfine-field distribution profile is bimodal (Figure 5b). The high-field maximum again can be attributed to a hematite phase while the second one remains unclear. The proportion of this sextet decreases in favor of the Fe^{3+} doublet upon increasing the measuring temperature, while for the latter a broadening of the quadrupole-splitting distribution toward higher values (Figure 5c and 5e) is obvious. The hematite contribution can thus be explained by the agglomeration of some Fe^{3+} ions in the corundum (α_1) lattice. From the MS recorded at temperatures exceeding 75 K, this sextet cannot be resolved in the fits. In addition, above 75 K, the contribution of the α-Fe sextet begins to decrease gradually with increasing temperature. This is compensated by an increase of the Fe^{3+} proportions while the Fe_3C and singlet proportions do not seem to be affected. This behavior cannot correspond to a phase transition but must be explained by a phenomenon related to the Mössbauer measurement itself. Zhang et al.[35] have described a similar absorption decrease in the MS of cementite particles with a diameter larger than 15 nm by vibration amplitudes in the order of Angströms because of their encapsulation in graphite. As shown later in the electron-microscopy section, TEM observations reveal that some particles with a diameter of about 20 nm are enclosed in the inner pores of the matrix. If we assume that these particles are α-Fe, enhanced vibration with increasing temperature could then explain the absorption decrease of the α-Fe sextet. If it

TABLE 2: MS Parameters of R800, R850, R910, R990, and R1070 Measured at 80 K[a]

	superpara Fe^{3+}				ferro α-Fe					ferro Fe_3C					nonf erro Fe		
	δ	ΔE_Q	Γ	P	δ	H_{hf}	$2\epsilon_Q$	Γ	P	δ	H_{hf}	$2\epsilon_Q$	Γ	P	δ	Γ	P
R800	0.39	0.54	0.36	80	0.11	341	0[b]	0.27	12	0.31[b]	247[b]	0[b]	0.77	6	0.19	0.17	2
R850	0.39	0.54	0.34	71	0.11	340	0[b]	0.21	8	0.31	246	0[b]	0.52	14	0.08	0.62	7
R910	0.39	0.53	0.36	59	0.12	338	0[b]	0.29	11.5	0.31	246	0[b]	0.38	18	0.03	0.55	11.5
R990	0.39	0.55	0.48	33	0.11	341	0[b]	0.37	25.5	0.30	248	0[b]	0.49	23	0.00	0.52	18.5
R1070	0.39	0.58	0.88	13	0.11	341	0[b]	0.31	32	0.31	249	0[b]	0.36	32	−0.02	0.43	23

[a] Superpara: superparamagnetic; ferro: ferromagnetic; H_{hf}: hyperfine field (kOe); δ: isomer shift (mm/s); ΔE_Q: quadrupole splitting (mm/s); $2\epsilon_Q$: quadrupole shift (mm/s); Γ: line width (mm/s); P: proportion (%). [b] Fixed parameter.

TABLE 3: MS Parameters of R800, R850, R910, R990, and R1070 Measured at RT[a]

	superpara Fe^{3+}				ferro α-Fe					ferro Fe_3C					nonf erro Fe		
	δ	ΔE_Q	Γ	P	δ	H_{hf}	$2\epsilon_Q$	Γ	P	δ	H_{hf}	$2\epsilon_Q$	Γ	P	δ	Γ	P
R800	0.30	0.53	0.34	81	0.00	330	0[b]	0.31	10.5	0.19[b]	206[b]	0.025[b]	0.83	5.5	−0.07	0.27	3
R850	0.29	0.54	0.32	71	0.00	330	0[b]	0.29	6	0.19	204	0.011	0.59	12.5	−0.04	0.79	10.5
R910	0.29	0.54	0.35	63	−0.01	329	0[b]	0.29	7	0.19	203	0.025	0.51	17.5	−0.11	0.56	12.5
R990	0.29	0.55	0.41	39	−0.01	327	0[b]	0.32	19	0.19	205	0.026	0.44	23	−0.13	0.42	19
R1070	0.30	0.56	0.78	17	−0.01	327	0[b]	0.34	27.5	0.19	207	0.025	0.30	31	−0.13	0.34	24.5

[a] Superpara: superparamagnetic; ferro: ferromagnetic; H_{hf}: hyperfine field (kOe); δ: isomer shift (mm/s); ΔE_Q: quadrupole splitting (mm/s); $2\epsilon_Q$: quadrupole shift (mm/s); Γ: line width (mm/s); P: proportion (%). [b] Fixed parameter.

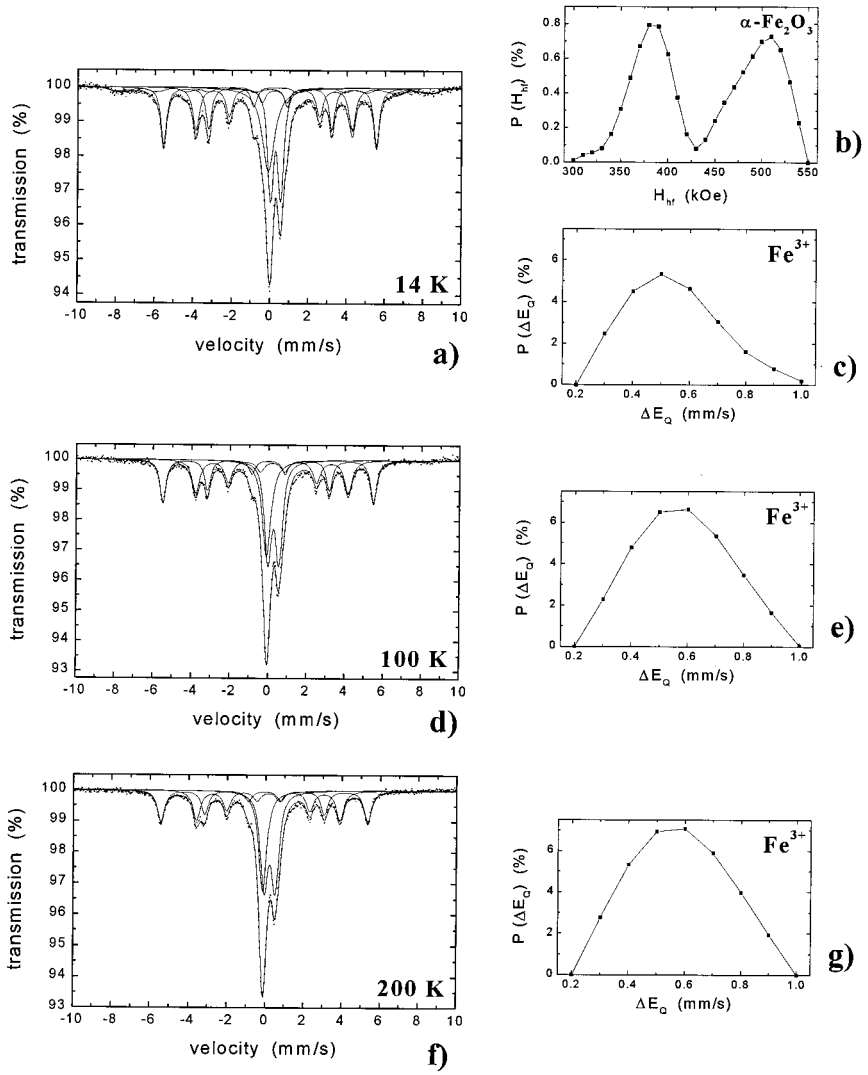

Figure 5. MS (a) and α-Fe_2O_3 hyperfine-field (b) and Fe^{3+} quadrupole-splitting (c) distributions of R990 measured at 14 K, MS (d) and Fe^{3+} quadrupole-splitting distribution (e) of R990 measured at 100 K and MS (f) and Fe^{3+} quadrupole-splitting distribution (g) of R990 measured at 200 K.

TABLE 4: MS Parameters of R990 Measured at Different Temperatures[a]

	superpara Fe^{3+c}				α-Fe_2O_3[d]					ferro α-Fe					ferro Fe_3C					nonfe rro Fe		
T (K)	$\bar{\delta}$	ΔE_Q	Γ	P	$\bar{\delta}$	H_{hf}	$\overline{2\epsilon_Q}$	Γ	P	δ	H_{hf}	$2\epsilon_Q$	Γ	P	δ	H_{hf}	$2\epsilon_Q$	Γ	P	δ	Γ	P
14	0.40	0.55	0.29	23	0.40	380 510	−0.09	0.34	9.5	0.11	344	0[b]	0.35	26	0.32	253	−0.01	0.41	22	0.00	0.77	19.5
30	0.39	0.50	0.29	24	0.36	380 515	−0.02	0.30	8	0.12	343	0[b]	0.35	25	0.32	252	−0.02	0.44	23	0.01	0.74	20
50	0.39	0.55	0.33	26.5	0.46	390 510	−0.10	0.12	5	0.12	342	0[b]	0.37	26	0.33	251	−0.01	0.43	22.5	0.02	0.64	20
75	0.38	0.55	0.33	28	0.41	390 490	−0.08	0.09	3	0.11	341	0[b]	0.37	26.5	0.31	250	−0.01	0.44	22.5	0.01	0.58	20
100	0.37	0.55	0.36	31						0.10	341	0[b]	0.38	25	0.30	247	−0.01	0.47	24	0.01	0.55	20
125	0.37	0.55	0.38	31.5						0.10	339	0[b]	0.40	25.5	0.29	244	−0.01	0.47	23.5	0.00	0.51	19.5
200	0.33	0.55	0.40	34						0.06	334	0[b]	0.44	23.5	0.25	232	0.01	0.46	22.5	−0.04	0.49	20
RT	0.28	0.55	0.39	37.5						−0.01	328	0[b]	0.46	20	0.18	206	0.02	0.48	23	−0.12	0.48	19.5

[a] Superpara: superparamagnetic; ferro: ferromagnetic; H_{hf}: hyperfine field (at the maxima of the distribution for[c]) (kOe); δ: (average) isomer shift (mm/s); ΔE_Q: quadrupole splitting at the maximum of the distribution.[b] (mm/s); $2\epsilon_Q$: (average) quadrupole shift (mm/s); Γ: Lorentzian line width (mm/s); P: proportion (%). [b] Fixed parameter. [c] Quadrupole-splitting distribution from 0.20 to 1.00 mm/s. [d] Hyperfine-field distribution from 300 to 550 kOe.

appears to be the best explanation, several remarks must, however, be made about this hypothesis. First, the size of the involved α-Fe particles, even if in agreement with Zhang et al.,[35] seems a bit large to the present authors. Second, it could be expected that the isomer-shift values of the α-Fe sextet would be affected by the particle vibrations, whereas they show a typical bulk α-Fe behavior. Third, the proportion decrease of the α-Fe sextet should affect the three other proportions of the MS and not only the Fe^{3+} doublet one. Concerning this last point, it can be suspected that another phenomenon is also involved. Indeed, in relation with the Debye temperature of the material, oxide phases may have a slightly different Mössbauer-

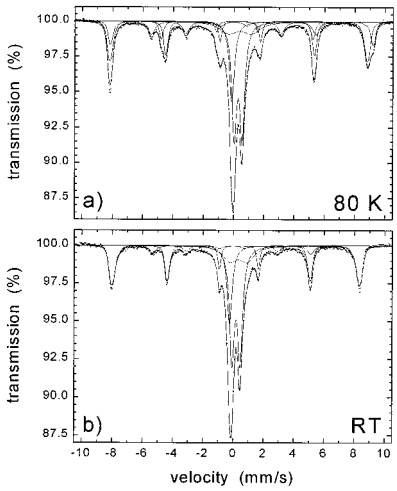

Figure 6. MS of R990ox measured at 80 K (a) and at RT (b).

fraction evolution with temperature as regards metallic phases, influencing also the measured proportions. In the following, the MS proportions given by the spectra at 80 K will be considered as the most representative (Figure 4a and Table 2).

The singlet exhibits a clear broadening at low temperatures. This is typical of γ-Fe showing an antiferromagnetic coupling at low temperatures.[36] The presence of γ-Fe at such a temperature can be explained by the small size of the particles[37] and by the presence of carbon atoms in the neighborhood of iron.[38] Indeed, γ-Fe particles have never been observed in Fe−Al_2O_3 powders prepared by reduction in pure H_2.[27,32,39,40] The singlet is therefore attributed to a γ-Fe−C alloy, in agreement with earlier results on CNTs-Fe−$MgAl_2O_4$ powders.[41]

With the aim to retrieve more information about the location of the different iron phases inside the matrix grains or on its surface, R990 was oxidized in air at 600 °C, and the MS of the resulting powder (denoted as R990ox in the following) were recorded at 80 K and at RT (Figure 6 and Table 5). Comparing the MS parameters of R990 and R990ox measured at 80 K (Tables 2 and 5), it appears that the Fe^{3+} proportion remains constant while the γ-Fe−C proportion slightly decreases and the α-Fe proportion considerably decreases. No more Fe_3C can be detected but two extra sextets and one extra doublet were included in the fit. The two sextets are both characteristic of an α-Fe_2O_3 phase showing the coexistence of antiferromagnetic ($2\epsilon_Q = 0.30$ mm/s) and weakly ferromagnetic α-Fe_2O_3 ($2\epsilon_Q = -0.10$ mm/s). This reflects either a size distribution of the α-Fe_2O_3 particles or a partial substitution of Al ions in α-Fe_2O_3.[42] The doublet is very broad, and its MS parameters are consequently not accurate. The quadrupole-shift value agrees with an $FeAl_2O_4$ phase, although the isomer-shift value is rather small for Fe^{2+} ions.[43] Comparing the MS of R990ox measured at 80 K with that at RT shows that the proportions of the γ-Fe−C singlet and of the $FeAl_2O_4$ doublet remain more or less constant while the proportion of α-Fe decreases similarly to what was observed for R990. At RT, only one α-Fe_2O_3 sextet is detected, showing a typical weak ferromagnetic phase ($2\epsilon_Q = -0.19$ mm/s). Moreover, the total proportion of hematite decreases between 80 K and RT in favor of the Fe^{3+} doublet, again suggesting a superparamagnetic behavior. It can thus be concluded that (i) the γ-Fe−C pattern corresponds mostly to particles that were protected from the oxidation and thus that are embedded inside the matrix grains[44] (note that this implies that some of the carbon formed by decomposition of CH_4 diffuses into the matrix and alloys with Fe, stabilizing the γ form), (ii) the Fe_3C particles are on the surface of the matrix grains, and (iii) the α-Fe particles are found both inside the matrix grains (mostly in the inner pores of the matrix as assumed hereabove) and on the surface of the grains.

These results allow us to propose some explanations for the evolution of the phase compositions with changing T_r on the basis of the Mössbauer results obtained at 80 K (Figure 4a and Table 2). It is obvious that the surface species are reduced before those located in the bulk of the corundum (α_1) lattice. For R800, the latter Fe^{3+} ions are mostly unreduced, and accordingly the proportion of the γ-Fe−C pattern is very low. For higher T_r, this proportion gradually increases showing the progressive reduction of the matrix (α_1 lattice). Note that, as indicated by the discrepancy of the α-Fe proportions between 80 K and RT, it was assumed that a fraction of the α-Fe also corresponds to particles dispersed in the inner porosity of the matrix. The remaining of the α-Fe pattern and the Fe_3C pattern correspond to surface particles. It is proposed that the α_2 particles are reduced into relatively large α-Fe particles (noted ex-α_2) and that the surface Fe^{3+} ions form smaller α-Fe particles (noted ex-Fe^{3+}), which can react with carbon and eventually form Fe_3C. For R800, the super-saturation of CH_4 in the reduction atmosphere is still low at that temperature and only a fraction of these ex-Fe^{3+} α-Fe particles form Fe_3C, whereas for higher T_r (specimens R850 and R910), they probably all form Fe_3C. For R850 and R910, the α-Fe proportion is indeed lower than for R800. It is proposed that the α-Fe pattern corresponds to the larger surface particles, that is, the larger ex-α_2 particles. For higher T_r (R990−R1070), the increase of the α-Fe proportion is mostly due to the formation of intragranular particles, and the increase of the Fe_3C proportion is mostly due to the transformation of the ex-Fe^{3+} α-Fe particles that are continuously produced at the surface of the matrix grains. The particles

TABLE 5: MS Parameters of R990ox Measured at 80 K and at RT[a]

	weakly ferro/antiferro α-Fe_2O_3										ferro α-Fe				
	$\overline{\delta}$		H_{hf}		$\overline{2\epsilon_Q}$		Γ		P		δ	H_{hf}	$2\epsilon_Q$	Γ	P
80 K	0.47[c]	0.47[c]	540[d]	530[d]	0.30	−0.10	0.25[c]	0.25[c]	12	23	0.09	337	0[b]	0.53	11
RT	0.36		510[f]		−0.19		0.23		29.5		0[b]	323	0[b]	0.50[b]	7

	para $FeAl_2O_4$				superpara Fe^{3+}				para γ-Fe-C		
	$\overline{\delta}$	ΔE_Q	Γ	P	Δ	ΔE_Q	Γ	P	δ	Γ	P
80 K	0.50	1.50[e]	1.39	11.5	0.39	0.52	0.38	30.5	−0.04	0.41	12
RT	0.44	1.10[g]	1.11	14	0.29	0.54	0.38	36	−0.14	0.40	13.5

[a] Ferro: ferromagnetic; para: paramagnetic; H_{hf}: hyperfine field at the maximum of the distribution (kOe); δ: (average) isomer shift (mm/s); ΔE_Q: quadrupole splitting at the maximum of the distribution (mm/s); $2\epsilon_Q$: (average) quadrupole shift (mm/s); Γ: Lorentzian line width (mm/s); P: proportion (%). [b] Fixed parameter. [c] Coupled parameters. [d] Hyperfine-field distribution from 500 to 550 kOe. [e] Quadrupole-splitting distribution from 1.20 to 2.20 mm/s. [f] Hyperfine-field distribution from 470 to 530 kOe. [g] Quadrupole-splitting distribution from 0.80 to 1.80 mm/s.

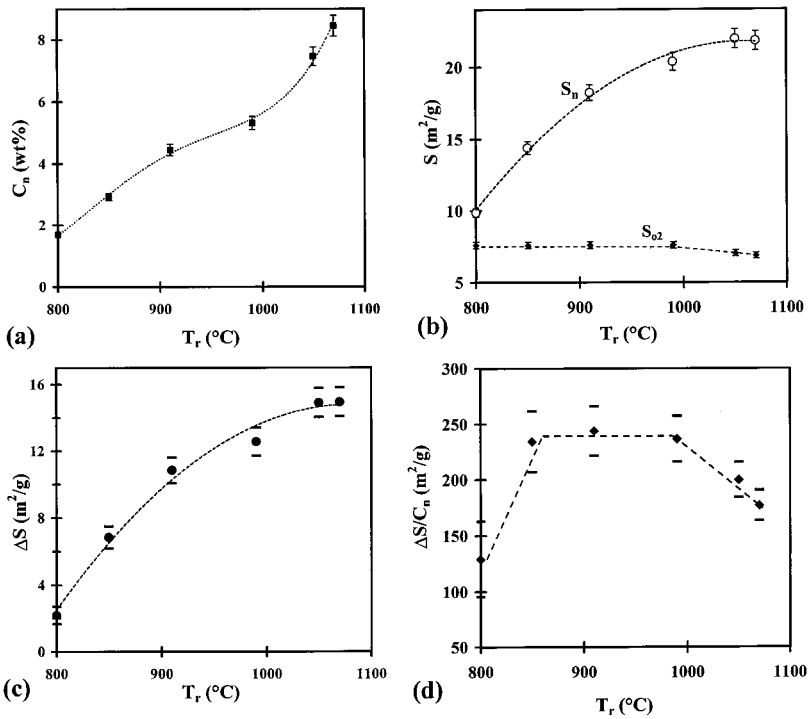

Figure 7. Carbon content (C_n) in the nanocomposite powders (a), specific surface area of the nanocomposite powders (S_n) and of the specimens oxidized in air (S_{o2}) (b), $\Delta S = S_n - S_{o2}$, representing the CNT quantity in the composite powders (c), $\Delta S/C_n$, representing the carbon quality in the composite powders (d). The dashed lines are guides to the eye.

TABLE 6: Carbon Content (C_n) and Specific Surface Areas[a] Characterizing the Composite Powders

	C_n (wt %)	S_n (m^2/g)	S_{o1} (m^2/g)	S_{o2} (m^2/g)	ΔS (m^2/g)	$\Delta S/C_n$ (m^2/g)
R800	1.7 ± 0.1	9.9	7.7	7.6	2.3 ± 0.5	134 ± 31
R850	2.9 ± 0.1	14.4	7.6	7.6	6.8 ± 0.7	233 ± 23
R910	4.4 ± 0.1	18.2	7.4	7.6	10.6 ± 0.8	239 ± 17
R990	5.3 ± 0.1	20.4	7.8	7.6	12.8 ± 0.8	240 ± 16
R1050	7.5 ± 0.2	21.9	7.1	7.0	14.9 ± 0.9	200 ± 10
R1070	8.5 ± 0.2	21.8	6.9	6.9	14.9 ± 0.9	177 ± 12

[a] S_n: value measured for the composite powder; S_{o1}: value measured for the powder oxidized at 900 °C; S_{o2}: value retained for the calculations; $\Delta S = S_n - S_{o2}$ represents the CNT quantity (see text); $\Delta S/C_n$ represents the carbon quality (see text).

that could be connected to the CNT formation are those located on the surface, and the above results show that the surface particles appear as α-Fe and Fe_3C in postreaction Mössbauer analysis. However, the surface α-Fe particles are relatively large, as indicated above, and it is unlikely that they would contribute to the CNT formation. This agrees with a previous study[41] on CNTs-Fe−$MgAl_2O_4$ showing that the particles responsible for the nucleation and possibly growth of the CNTs are found as Fe_3C by postreaction Mössbauer analysis. The exact nature of the catalytic particle is not known but it is probably a very small carbon-containing (ex-Fe^{3+}) Fe particle in which some still poorly established driving forces make carbon atoms to participate in the CNT formation. The catalytic particle would evolve toward the Fe_3C form only after termination of the CNT growth. However, it was also shown[41] that some of the surface particles that were inactive for the CNT formation also end up as Fe_3C.

Carbon Content and Specific Surface Areas. The carbon content (C_n – Table 6 and Figure 7a) increases with T_r from 1.7 wt % (R800) to 8.5 wt % (R1070). The specific surface area of the nanocomposite powders (S_n, Table 6 and Figure 7b) is higher than the specific surface area of the starting solid solution (9.0 ± 0.3 m^2/g) and increases with T_r. As pointed out earlier,[4,6,28] it is the deposition of carbon in the composite powder, particularly in the form of CNTs, which is responsible for most of this supplementary surface area. The Fe or Fe_3C particles located at the surface of the matrix grains can also contribute to this increase of surface area, but only to a much smaller extent. After all the carbon is eliminated by air oxidation at 900 °C, the specific surface area of the resulting powders is measured (S_{o1} – Table 6). S_{o1} for the powders R800 − R990 can be considered as equal to $S_{o2} = 7.6$ m^2/g, which will be used for further calculations (Table 6). Since for these powders, the reduction is performed at a temperature lower than that (1000 °C) used for the calcination of the solid solution, it is a reasonable assumption that only a little sintering of the matrix grains occurred during the reduction thermal treatment. In contrast, for R1050 and R1070, S_{o1} is lower than for the previous powders, which could indicate that a significant sintering of the matrix grains has taken place during the reduction. Thus, S_{o2} values will be taken as equal to S_{o1} values for these powders. S_{o2} values are plotted in Figure 7b. As proposed in previous works,[4,6,28] $\Delta S = S_n - S_{o2}$ (Table 6 and Figure 7c) represents the surface area of the carbon present in the nanocomposite powder, which essentially corresponds to that of the CNTs. Thus the evolution of ΔS reflects the increasing quantity of CNTs (more precisely of nanotube bundles) with increasing T_r. This is in good qualitative agreement with the above observation that the reduction yield increases with T_r, and thus that there are more catalyst particles, and also with the increase of the proportion of particles detected as Fe_3C in postreaction MS analysis.

$\Delta S/C_n$ (Table 6 and Figure 7d) can be considered as a quality data,[4,6,28] a higher figure for $\Delta S/C_n$ essentially denoting more carbon in tubular form or tubes with fewer walls, or bundles made up of less CNTs (i.e., smaller diameter bundles). $\Delta S/C_n$

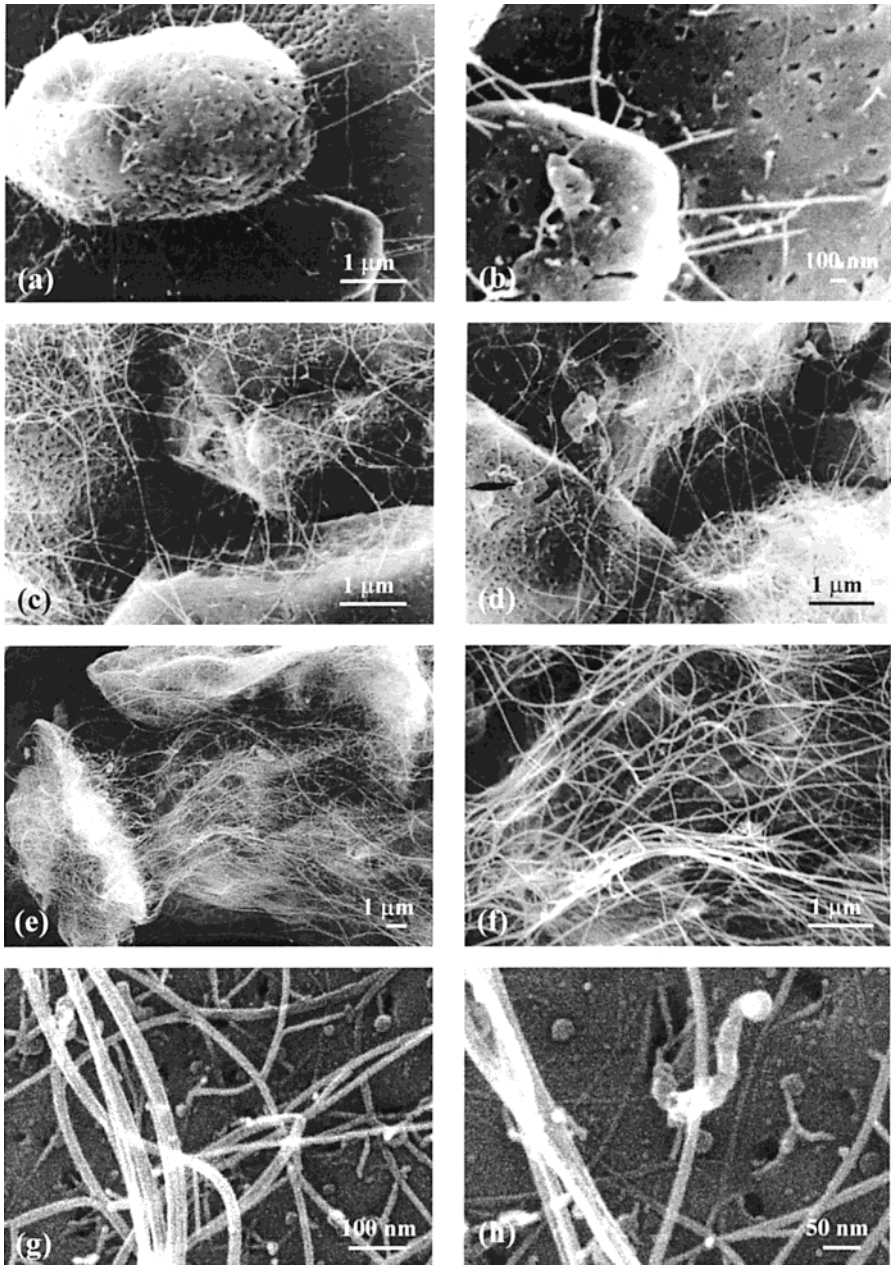

Figure 8. SEM images of R850 (a, b), R910 (c), R990 (d), R1070 (e), and SEM−FEG images of the carbon species at the surface of a matrix grain in R990 (e, f).

increases from R800 to R850, reaching a plateau at R850−R990, and decreases for R1050 and R1070. As observed in earlier studies,[5−9,15] the maximum of the quantity parameter is not simultaneously obtained with the maximum of the quality parameter. Electron microscopy observations presented in the following section may help to give a better understanding on the evolutions of ΔS and $\Delta S/C_n$.

Electron Microscopy. SEM images of carbon filaments at the surface of the matrix grains in R850, R910, R990 and R1070 are shown in Figure 8. TEM studies on similar powders[4−7,15] have demonstrated that these filaments are mostly bundles of CNTs. The observations show that the quantity of bundles increases with increasing T_r, in agreement with the above macroscopical study. No bundles were detected in R800. Some bundles are observed in R850 (Figure 8a) and are connected to the matrix grains at their two tips (Figure 8b). The small species appearing as white dots or elongated dots at the grain surfaces (Figure 8b) are either Fe/Fe_3C particles or very short CNTs. In R910 (Figure 8c) and R990 (Figure 8d), the CNTs bundles are much more numerous and are also long. A weblike network of bundles thus covers the matrix grains. In R1070 (Figure 8e and f), the CNTs bundles are thicker (up to about 50 nm in diameter) and the network is more dense. On higher resolution images of R990 obtained with a field-effect-gun microscope (SEM-FEG) (Figure 8g and h), it is possible to resolve individual CNTs about 5 nm in diameter either isolated or within a bundle (Figure 8g). Spherical Fe or Fe_3C particles are revealed at the matrix surface (Figure 8h). The diameter of these particles falls into one of two populations: not larger than 5−6 nm or in the range 25−40 nm. The former are ex-Fe^{3+} particles and the latter are ex-α_2 particles. Figure 8h also shows a short fiber, about 30 nm thick, the formation of which was catalyzed by an ex-α_2 large particle that seems to be located at the tip. Such a short, thick fiber is similar to some species commonly observed in works on filamentous carbon[3]. Its formation mechanism is different from those thought to occur in the case of CNTs.

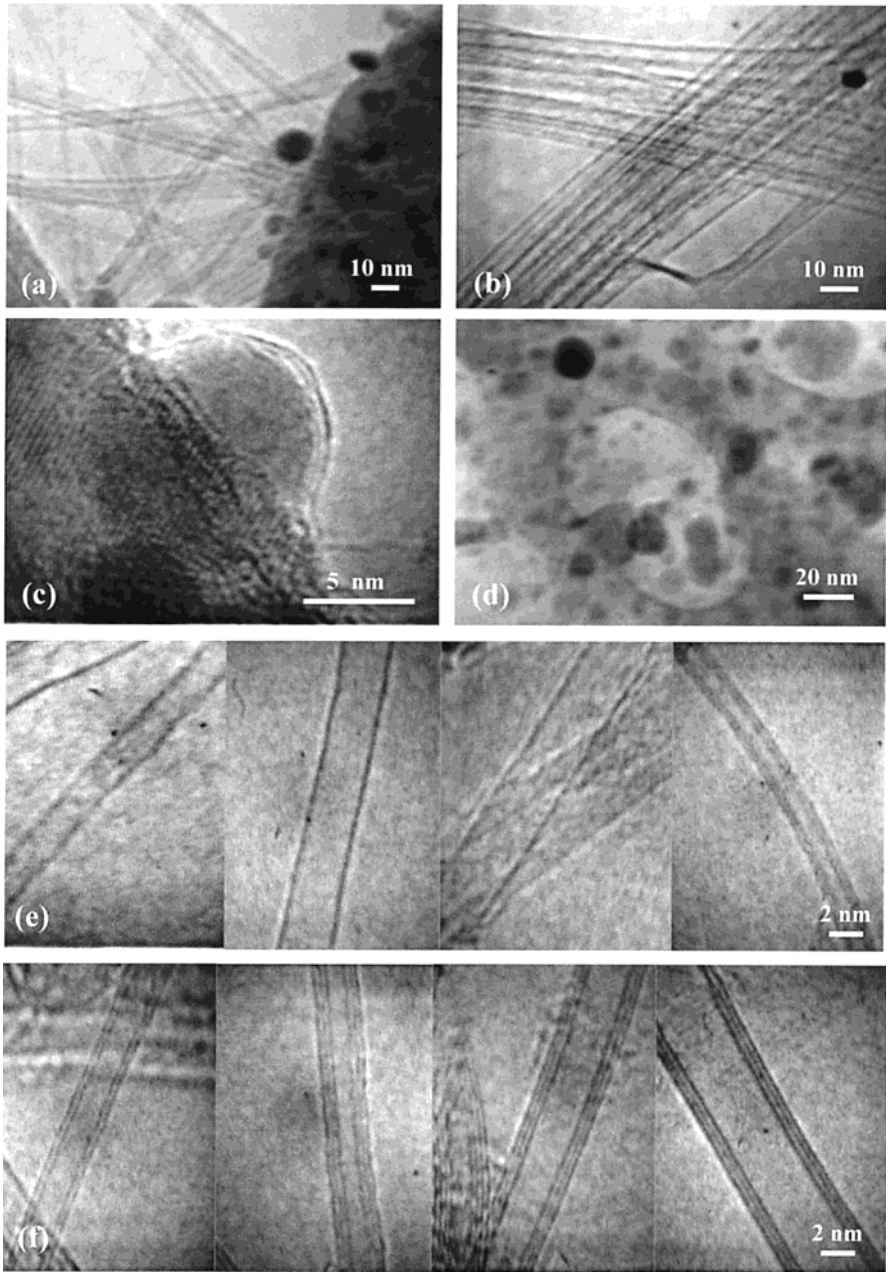

Figure 9. TEM (a−d) and HREM (e−f) images of composite powders: individual CNTs, some Fe and Fe_3C particles and part of a matrix grain (R990 − a), 2 bundles of CNTs (R1070 − b), an Fe or Fe_3C particle covered of 2 or 3 graphene layers (R990 − c), some Fe or Fe_3C particles located within a matrix grain or at the matrix grain surface (R1070 − d), SWNTs, DWNTs, and 3WNTs with external diameter in the 1.5−6 nm range (e, f).

TEM and HREM images of R850, R990, and R1070 are shown in Figure 9. It is noteworthy that no amorphous carbon coating of the CNTs is observed. On Figure 9a (R990), many individual CNTs (2−5 nm in diameter) are observed together with a matrix grain and some Fe and Fe_3C particles (2−12 nm in diameter). Two intersecting bundles are shown in Figure 9b (R1070). Figure 9c (R990) shows an Fe or Fe_3C particle, 10 nm in diameter, partially superimposed with a matrix grain. The particle is too large to have been active for the catalytic growth of a CNT and has been encapsulated by two graphene sheets. Such individual CNTs, bundles of CNTs, and Fe or Fe_3C particles have been observed on all three powders. However, the proportion of bundles versus that of individual CNTs is small for R850, larger for R990, and much larger for R1070. Indeed, the increase in the CNT quantity favors bundling, which may contribute to the decrease of $\Delta S/C_n$ as noted above (Figure 7d). Observation of the matrix grains (Figure 9d) reveals that many inner pores contain Fe particles larger ($\geq$20 nm) than those located at an intragranular position ($<$5 nm). Each large particle is produced by the coalescence of several smaller ones inside the inner pore. The presence of such particles could account for some data presented in the above Mössbauer spectroscopy section. The CNTs shown on HREM images (Figure 9e and f) are representative of the individual CNTs observed in the different powders. Three SWNTs (1.7, 2.7, and 3.2 nm in diameter, respectively) and one small DWNT (1.8 nm in outer diameter) are shown in Figure 9e. One DWNT (2.1 nm in outer diameter) and three three-walls-CNTs (3WNTS, 2.5, 3.7, and 4.8 nm in diameter, respectively) are shown in Figure 9f. CNTs with 4−6 walls were very marginally observed. Bundles of very small SWNTs (0.7 nm) as those reported by Colomer et al.[20,21] were not observed, indicating that the involved mechanism,

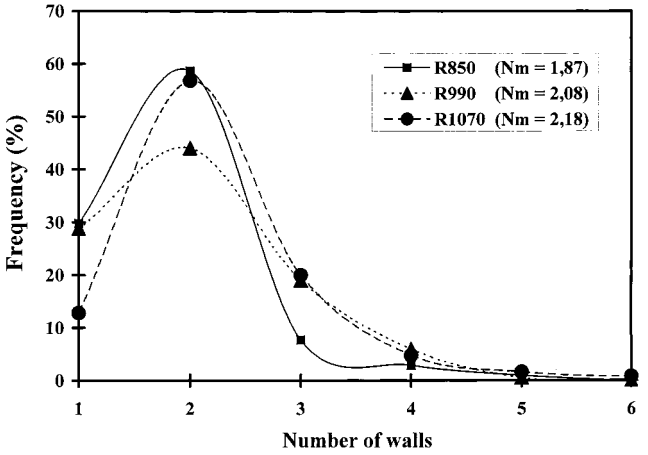

Figure 10. Distributions of the numbers of walls of the CNTs in R850, R990, and R1070 conducted on the HREM images (typically as those shown in Figure 9) of 100, 167, and 111 CNTs, respectively.

where bundles grow from a single bigger catalyst particle, is not operative in the present experimental conditions.

However, it is not possible to determine the variation of the CNT characteristics from a sample to another from the observation of only a few images. Thus, more than 100 images of CNTs for each of the three powders R850, R990, and R1070 were captured, allowing a statistical study. The distributions of the numbers of walls (Figure 10) show that most CNTs are SWNTs or DWNTs. Indeed, for R850, the sum of the proportions of SWNTs and DWNTs is higher than 90%. It decreases to 73% for R990, which contains less DWNTs and more 3WNTs and 4WNTs than R850, and to 70% for R1070, which contains less SWNTs and more 3WNTs and 4WNTs than R850. Note that the difference between R990 (73%) and R1070 (70%) is small. The average number of walls was calculated (N_m in Figure 10), but note that it is only a statistical parameter since it is not an integer. The trend is clearly that N_m increases with T_r (from 1.87 to 2.08 and to 2.18 for R850, R990, and R1070). This could reflect the thickening of the CNTs by formation of additional walls with increasing T_r or the formation of CNTs with more walls from the freshly formed catalyst particles.

The distributions of the diameters of SWNTs and of the inner diameters of DWNTs and 3WNTs are plotted in Figure 11 for each of the three powders R850, R990, and R1070. The width of the diameter distributions for the SWNTs in R850 and R990 is similar to that (1−5 nm) reported for SWNTs prepared by catalytic methods.[13,14,17,20,22−25] The peak in the distribution is rather narrow, 70% of the SWNTs being between 2 and 3.2 nm in diameter (i.e., within one of the classes 2.2, 2.6, and 3.0 nm), which is markedly higher than the peak usually reported (1.2−1.7 nm). As pointed out by Dai et al.,[17] a distribution in tube diameter reflects a mechanism in which the diameter is established by the catalytic particle. The present diameter distribution is in excellent agreement with the theoretical and experimental results[14] showing that catalyst particles below ca. 3 nm in diameter produce CNTs while larger particles are encapsulated.

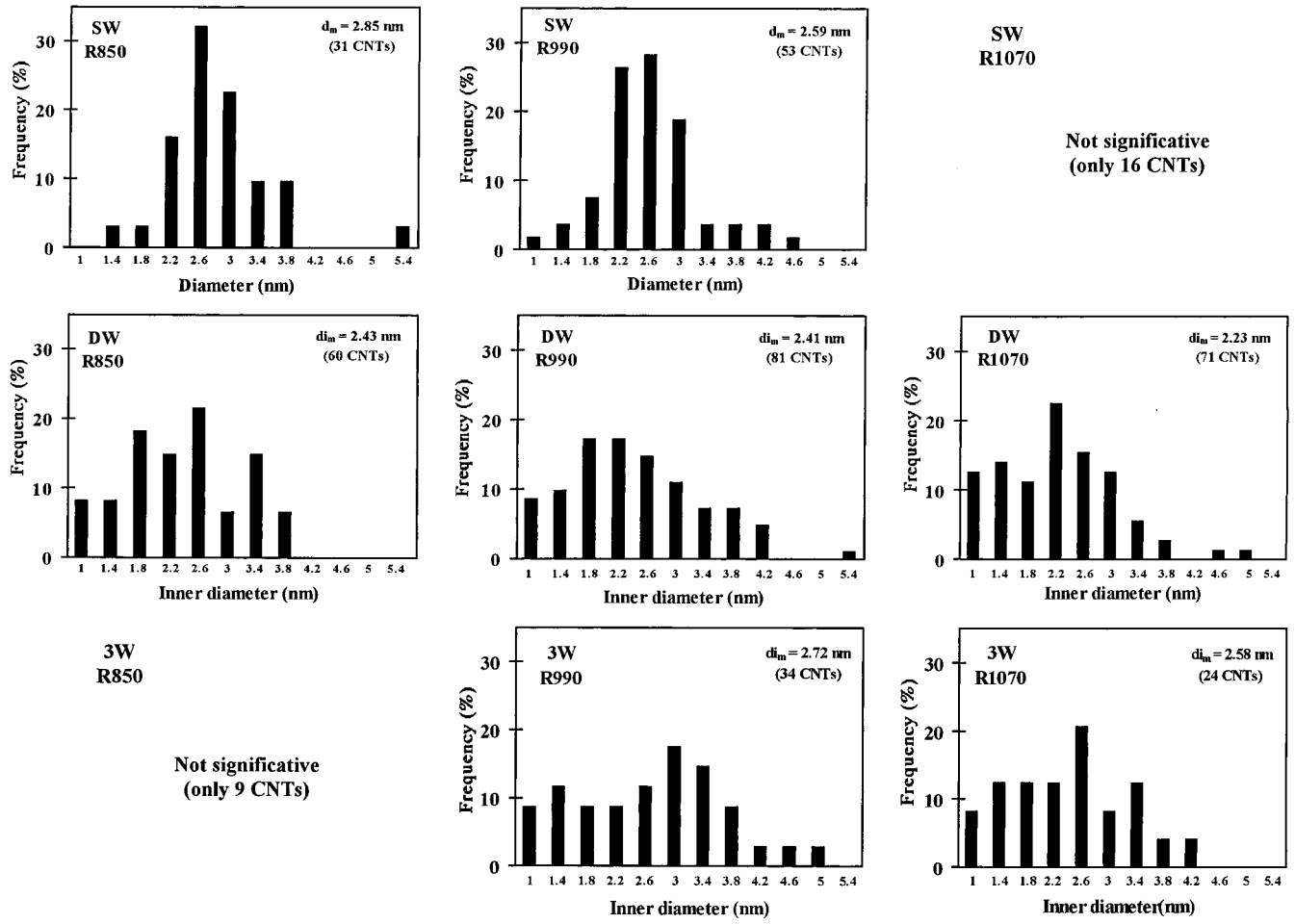

Figure 11. Diameter distributions of SWNTs and inner-diameter distributions of DWNTS and 3WNTs in R850, R990, and R1070, successively, measured on HREM images (typically as those shown in Figure 9). Each class noted by a value x nm corresponds to CNTs (inner) diameters contained between $x - 0.2$ nm and $x + 0.2$ nm.

By contrast, the inner diameter distributions of the DWNTs and 3WNTs are larger. For DWNTs and 3WNTs, as opposed to SWNTs, a large proportion (>30%) of the inner diameters is within the smaller diameter classes (i.e., 1.0, 1.4, and 1.8 nm). Two explanations could be proposed. First, this could reflect the internal growth of the second wall, possibly by the yarmulke mechanism.[17] A characteristic of this mechanism is that the outermost layer grows first. A second carbon cap (yarmulke) can form underneath the first, spaced by roughly the interlayer spacing of graphite and forcing it to lift up by forming a tube whose open end remains chemisorbed to the catalytic particle. Second, another phenomenon is that at a given T_r, the smaller catalytic particles (<2 nm) are more active than the larger ones because of a higher surface curvature and thus produce more carbon more rapidly, and therefore could tend to form DWNTs rather than SWNTs.

Comparing the inner diameters for DWNTs and 3WNTS (for powder R990) shows that the distribution is less skewed toward the small diameters for 3WNTS. This indicates that the third wall forms outside, probably because the increased curvature involved in an inner nucleation would impose too great of a strain. The values found for the inner diameters are nevertheless much smaller than those reported elsewhere.[17,45] Furthermore, for a given T_r, many DWNTs and 3WNTs have an inner diameter in the same range of the diameters of SWNTs, showing that an outer growth of the second and third walls also occurs. In fact, the enlargement of the diameter distribution suggests that several base-growth mechanisms of CNTs simultaneously operate, depending on the actual characteristics of the involved catalytic nanoparticle and also of the temperature.

From R850 to R990, the average diameter of SWNTs (d_m, Figure 11) decreases from 2.85 to 2.59 nm. Similarly, from R850 to R1070, the average inner diameter (di_m, Figure 11) for DWNTs decreases from 2.43 to 2.23 nm, and the same evolution is observed from R990 to R1070 for 3WNTs (from 2.72 to 2.58 nm). It is thought that the diameter of a particle catalytically active for the formation of a CNT is about that of the inner diameter of the produced CNT. For a MWNT, the particle can be about 0.64 nm larger than the inner diameter only when the internal growth of the second wall occurs. More metal particles are generated because of the increased reduction yield when using a higher T_r. Both the increase of the quantity parameter (ΔS, Table 6 and Figure 7c) and the SEM observations (Figure 8) have shown that the CNT formation has already started at 850 °C and that it continues during the ramp up to the target temperature. It may then be thought that the metal particles would be more prone to grow or coalesce, and thus to catalyze the formation of larger CNTs. In the present case, it seems that this does not take place. It is proposed that because of the higher super-saturation level of CH_4 in the gas atmosphere with increasing T_r, more carbon is immediately made available to the native particles. As soon as they are catalytically active and start growing a tube, the particles stop their growth. Only some CNTs observed in R1070 are actually formed at temperatures close to 1070 °C, and we thus infer that the latest CNTs have very small inner diameters perhaps smaller than 2 nm. However, the higher super-saturation level of CH_4 also favors the formation of outer layers on previously grown CNTs, accounting for the fact that more 3WNTs (and less SWNTs) are observed for R1170 than for R850 (Figure 11). But the above observation that the proportion of CNTs with three walls or more is not markedly lower for R1070 than for R990 indicates that this latter phenomenon (outer layer formation) is less active than the former one (formation of new, very small CNTs). Of course, this is valid only if the feedstock for metal particles is not exhausted, that is, if Fe^{3+} ions remain available for reduction in the oxide matrix lattice.

Conclusions

The reduction in H_2/CH_4 atmosphere of aluminum−iron oxides produces metal particles, which are small enough to catalyze the formation of single-walled carbon nanotubes. Several experiments have been made using the same temperature profile and changing only the maximum temperature (800−1070 °C). Characterizations of the catalyst material before and after the reactions are performed using chiefly ^{57}Fe Mössbauer spectroscopy. Electron microscopy and a macroscopical method are used to characterize the nanotubes. The nature of the iron species (Fe^{3+}, α-Fe, Fe_3C, γ-Fe−C) is correlated to their location in the material. The particles responsible for the nucleation and possibly growth of the carbon nanotubes are probably an Fe−C alloy but are found as Fe_3C by postreaction Mössbauer analysis. Increasing the reduction temperature increases the reduction yield and thus favors the formation of surface metal particles, thus producing more carbon nanotubes. The carbon nanotubes are found mostly as single-walled and double-walled tubes with an average diameter close to 2.5 nm. Several formation mechanisms of the base-growth kind are thought to be active. In particular, it is shown that the second wall can grow inside the first one but that subsequent ones are formed outside. It is also possible that under given experimental conditions, the smallest (<2 nm) catalyst particles are more active and preferentially produce double-walled tubes rather than single-walled tubes.

Acknowledgment. The authors would like to thank Mr. L. Datas for his assistance in the TEM and HREM observations, which have been performed at the "Service Commun de Microscopie Electronique à Transmission − Université Paul-Sabatier". This research is supported by the Belgian National Program of Inter-University Attraction Pole on Reduced Dimensionality Systems (P4/10), by the Fund for Scientific Research − Flanders, and by the Franco-Belgian TOURNESOL program (T99/006-T99/045).

References and Notes

(1) Iijima, S. *Nature (London)* **1991**, *354*, 56.
(2) Laurent, Ch.; Flahaut, E.; Peigney, A.; Rousset, A. *New J. Chem.* **1998**, *22*, 1229.
(3) Rodriguez, N. M. *J. Mater. Res.* **1993**, *8*, 3233.
(4) Peigney, A.; Laurent, Ch.; Dobigeon, F.; Rousset, A. *J. Mater. Res.* **1997**, *12*, 613.
(5) Peigney, A.; Laurent, Ch.; Dumortier, O.; Rousset, A. *J. Eur. Ceram. Soc.* **1998**, *18*, 1995.
(6) Laurent, Ch.; Peigney, A.; Rousset, A. *J. Mater. Chem.* **1998**, *8*, 1263.
(7) Laurent, Ch.; Peigney, A.; Flahaut, E.; Rousset, A. *Mater. Res. Bull.* **2000**, *35*, 661.
(8) Govindaraj, A.; Flahaut, E.; Laurent, Ch.; Peigney, A.; Rousset, A.; Rao, C. N. R. *J. Mater. Res.* **1999**, *14*, 2567.
(9) Flahaut, E.; Govindaraj, A.; Peigney, A.; Laurent, Ch.; Rousset, A.; Rao, C. N. R. *Chem. Phys. Lett.* **1999**, *300*, 236.
(10) Laurent, Ch.; Peigney, A.; Dumortier, O.; Rousset, A. *J. Eur. Ceram. Soc.* **1998**, *18*, 2005.
(11) Flahaut, E.; Peigney, A.; Laurent, Ch.; Chastel, F.; Marliere, Ch.; Rousset, A. *Acta Mater.* **2000**, *48*, 3803.
(12) Flahaut, E.; Peigney, A.; Laurent, Ch.; Rousset, A. *J. Mater. Chem.* **2000**, *10*, 249.
(13) Bacsa, R. R.; Laurent, Ch.; Peigney, A.; Bacsa, W. S.; Vaugien, Th.; Rousset, A. *Chem. Phys. Lett.* **2000**, *323*, 566.
(14) Hafner, J. H.; Bronikowski, M. J.; Azamian, B. K.; Nikolaev, P.; Rinzler, A. G.; Colbert, D. T.; Smith, K. A.; Smalley, R. E. *Chem. Phys. Lett.* **1998**, *296*, 195.

(15) Peigney, A.; Laurent, Ch.; Rousset, A. *J. Mater. Chem.* **1998**, *9*, 1167.
(16) Flahaut, E.; Peigney, A.; Laurent, Ch.; Rousset, A. to be published.
(17) Dai, H.; Rinzler, A. G.; Nikolaev, P.; Thess, A.; Colbert, D. T., Smalley, R. E. *Chem. Phys. Lett.* **1996**, *260*, 471.
(18) Ivanov, V.; Fonseca, A.; Nagy, J. B.; Lucas, A.; Lambin, P.; Bernaerts, D.; Zhang, X. B. *Carbon* **1995**, *33*, 1727.
(19) Hernadi, K.; Fonseca, A.; Nagy, J. B.; Bernaerts, D.; Lucas, A *Carbon* **1996**, *34*, 1249.
(20) Colomer, J. F.; Bister, G.; Willems, I.; Konya, Z.; Fonseca, A.; Van Tendeloo, G.; Nagy, J. B. *Chem. Commun*. **1999**, 1343.
(21) Colomer, J. F.; Stephan, C.; Lefrant, S.; Van Tendeloo, G.; Willems, I.; Konya, Z.; Fonseca, A.; Laurent, Ch.; Nagy, J. B. *Chem. Phys. Lett.* **2000**, *317*, 83.
(22) Cassell, A. M.; Raymakers, J. A.; Kong, J.; Dai, H. *J. Phys. Chem*. **1999**, *103*, 6484.
(23) Kong, J.; Cassell, A. M.; Dai, H. *Chem. Phys. Lett.* **1998**, *292*, 567.
(24) Su, Ming; Zheng, Bo; Lu, Jie. *Chem. Phys. Lett.* **2000**, *322*, 321.
(25) Cheng, H. M.; Li, F.; Sun, X.; Brown, S. D. M.;, Pimenta, M. A.; Marucci, A.; Dresselhaus, G.; Dresselhaus, M. S. *Chem. Phys. Lett.* **1998**, *289*, 602.
(26) Wagman, D. D.; Kilpatrick, J. E.; Taylor, W. J.; Pitzer, K. S.; Rossini, F. D. *J. Res. Natl. Bur. Stand.* **1945**, *34*, 143.
(27) Devaux, X.; Laurent, Ch.; Rousset, A. *Nanostruct. Mater*. **1993**, *2*, 339.
(28) Peigney, A.; Laurent, Ch.; Flahaut, E.; Bacsa, R. R.; Rousset, A. *Carbon* **2001**, *39*, 507.
(29) Muan, A.; Gee, C. L. *J. Am. Ceram. Soc*. **1956**, *39*, 207.
(30) Meyers, C. E.; Mason, T. O.; Petuskey, W. T.; Halloran, J. W.; Bowen, H. K. *J. Am. Ceram. Soc.* **1980**, *63*, 659.
(31) Polli, A. D.; Lange, F. F.; Levi, C. G.; Mayer, J. *J. Am. Ceram. Soc.* **1996**, *79*, 1745.
(32) Laurent, Ch.; Rousset, A.; Verelst, M.; Kannan, K. R.; Raju, A. R.; Rao, C. N. R. *J. Mater. Chem.* **1993**, *3*, 513.
(33) Vandenberghe, R. E.; De Grave, E.; Landuydt, C.; Bowen, L. H. *Hyperfine Interact.* **1990**, *53*, 175.
(34) Bi, X. X.; Ganguly, B.; Huffman, G. P.; Huggins, F. E.; Endo, M.; Eklund, P. C. *J. Mater. Res*. **1993**, *8*, 1666.
(35) Zhang, G. L.; du Marchie van Voorthuysen, E. H.; Szymanski, K.; Boom, G.; Verwerft, M. G. M.; Jonkman, H. T.; Niesen, L. *Il Nuovo Cimento* **1996**, *18D*, 281.
(36) Weiss, R. J. *Proc. Phys. Soc*. **1963**, *82*, 281.
(37) Kachi, S.; Bando, Y.; Higuchi, S. *Jpn. J. Appl. Phys*. **1962**, *1*, 307.
(38) Ron, M. In *Applications of Mössbauer Spectroscopy*; Cohen, R. L., Ed.; Academic Press: New York, **1980**; Vol. II, p 335.
(39) Marchand, A.; Barbara, B.; Mollard, P.; Fillion, G.; Devaux, X.; Rousset, A. *J. Magn. Magn. Mater*. **1992**, *116*, 64.
(40) Marchand, A.; Devaux, X.; Barbara, B.; Mollard, P.; Brieu, M.; Rousset, A. *J. Mater. Sci.* **1993**, *28*, 2217.
(41) Coquay, P.; De Grave, E.; Vandenberghe, R. E.; Dauwe, C.; Flahaut, E.; Laurent, Ch.; Peigney, A.; Rousset, A. *Acta Mater.* **2000**, *48*, 3015.
(42) Vandenberghe, R. E.; Van San, E.; Da Costa, G. M.; De Grave, E. *Czech J. Phys.* **2001**, in press.
(43) Larsson, L.; O'Neill, H. St. C.; Annersten, H. *Eur. J. Mineral.* **1994**, *6*, 39.
(44) Laurent, Ch.; Blaszczyk, Ch.; Brieu, M.; Rousset, A. *Nanostruct. Mater.* **1995**, *6*, 317.
(45) Tibbetts, G. G. *J. Cryst. Growth.* **1984**, *66*, 632.